Experimental Study of Hard Photon Radiation Processes at HERA

H1 Collaboration

Abstract:

We present an experimental study of the $ep \rightarrow e\gamma + p$ and $ep \rightarrow e\gamma + X$ processes using data recorded by the H1 detector in 1993 at the electron-proton collider HERA. These processes are employed to measure the luminosity with an accuracy of 4.5 %. A subsample of the $ep \rightarrow e\gamma + X$ events in which the hard photon is detected at angles $\theta'_\gamma \leq 0.45$ mrad with respect to the incident electron direction is used to verify experimentally the size of radiative corrections to the $ep \rightarrow eX$ inclusive cross section and to investigate the structure of the proton in the Q^2 domain down to 2 GeV^2, lower than previously attained at HERA.

H1 Collaboration

T. Ahmed[3], S. Aid[13], V. Andreev[24], B. Andrieu[28], R.-D. Appuhn[11], M. Arpagaus[36],
A. Babaev[26], J. Baehr[35], J. Bán[17], P. Baranov[24], E. Barrelet[29], W. Bartel[11], M. Barth[4],
U. Bassler[29], H.P. Beck[37], H.-J. Behrend[11], A. Belousov[24], Ch. Berger[1], H. Bergstein[1],
G. Bernardi[29], R. Bernet[36], G. Bertrand-Coremans[4], M. Besançon[9], R. Beyer[11],
P. Biddulph[22], J.C. Bizot[27], V. Blobel[13], K. Borras[8], F. Botterweck[4], V. Boudry[28],
A. Braemer[14], F. Brasse[11], W. Braunschweig[1], V. Brisson[27], D. Bruncko[17], C. Brune[15],
R. Buchholz[11], L. Büngener[13], J. Bürger[11], F.W. Büsser[13], A. Buniatian[11,39], S. Burke[18],
G. Buschhorn[26], A.J. Campbell[11], T. Carli[26], F. Charles[11], D. Clarke[5], A.B. Clegg[18],
B. Clerbaux[4], M. Colombo[8], J.G. Contreras[8], C. Cormack[19], J.A. Coughlan[5],
A. Courau[27], Ch. Coutures[9], G. Cozzika[9], L. Criegee[11], D.G. Cussans[5], J. Cvach[30],
S. Dagoret[29], J.B. Dainton[19], M. Danilov[23], W.D. Dau[16], K. Daum[34], M. David[9],
E. Deffur[11], B. Delcourt[27], L. Del Buono[29], A. De Roeck[11], E.A. De Wolf[4],
P. Di Nezza[32], C. Dollfus[37], J.D. Dowell[3], H.B. Dreis[2], A. Droutskoi[23], J. Duboc[29],
D. Düllmann[13], O. Dünger[13], H. Duhm[12], J. Ebert[34], T.R. Ebert[19], G. Eckerlin[11],
V. Efremenko[23], S. Egli[37], H. Ehrlichmann[35], S. Eichenberger[37], R. Eichler[36], F. Eisele[14],
E. Eisenhandler[20], R.J. Ellison[22], E. Elsen[11], M. Erdmann[14], W. Erdmann[36], E. Evrard[4],
L. Favart[4], A. Fedotov[23], D. Feeken[13], R. Felst[11], J. Feltesse[9], J. Ferencei[15],
F. Ferrarotto[32], K. Flamm[11], M. Fleischer[26], M. Flieser[26], G. Flügge[2], A. Fomenko[24],
B. Fominykh[23], M. Forbush[7], J. Formánek[31], J.M. Foster[22], G. Franke[11], E. Fretwurst[12],
E. Gabathuler[19], K. Gabathuler[33], K. Gamerdinger[26], J. Garvey[3], J. Gayler[11],
M. Gebauer[8], A. Gellrich[11], H. Genzel[1], R. Gerhards[11], U. Goerlach[11], L. Goerlich[6],
N. Gogitidze[24], M. Goldberg[29], D. Goldner[8], B. Gonzalez-Pineiro[29], I. Gorelov[23],
P. Goritchev[23], C. Grab[36], H. Grässler[2], R. Grässler[2], T. Greenshaw[19],
G. Grindhammer[26], A. Gruber[26], C. Gruber[16], J. Haack[35], D. Haidt[11], L. Hajduk[6],
O. Hamon[29], M. Hampel[1], E.M. Hanlon[18], M. Hapke[11], W.J. Haynes[5],
J. Heatherington[20], G. Heinzelmann[13], R.C.W. Henderson[18], H. Henschel[35], R. Herma[1],
I. Herynek[30], M.F. Hess[26], W. Hildesheim[11], P. Hill[5], K.H. Hiller[35], C.D. Hilton[22],
J. Hladký[30], K.C. Hoeger[22], M. Höppner[8], R. Horisberger[33], V.L. Hudgson[3], Ph. Huet[4],
M. Hütte[8], H. Hufnagel[14], M. Ibbotson[22], H. Itterbeck[1], M.-A. Jabiol[9],
A. Jacholkowska[27], C. Jacobsson[21], M. Jaffre[27], J. Janoth[15], T. Jansen[11], L. Jönsson[21],
K. Johannsen[13], D.P. Johnson[4], L. Johnson[18], H. Jung[29], P.I.P. Kalmus[20], D. Kant[20],
R. Kaschowitz[2], P. Kasselmann[12], U. Kathage[16], J. Katzy[14], H.H. Kaufmann[35],
S. Kazarian[11], I.R. Kenyon[3], S. Kermiche[25], C. Keuker[1], C. Kiesling[26], M. Klein[35],
C. Kleinwort[13], G. Knies[11], W. Ko[7], T. Köhler[1], J. Köhne[26], H. Kolanoski[8], F. Kole[7],
S.D. Kolya[22], V. Korbel[11], M. Korn[8], P. Kostka[35], S.K. Kotelnikov[24],
T. Krämerkämper[8], M.W. Krasny[6,29], H. Krehbiel[11], D. Krücker[2], U. Krüger[11],
U. Krüner-Marquis[11], J.P. Kubenka[26], H. Küster[2], M. Kuhlen[26], T. Kurča[17],
J. Kurzhöfer[8], B. Kuznik[34], D. Lacour[29], F. Lamarche[28], R. Lander[7], M.P.J. Landon[20],
W. Lange[35], P. Lanius[26], J.-F. Laporte[9], A. Lebedev[24], C. Leverenz[11], S. Levonian[24],
Ch. Ley[2], A. Lindner[8], G. Lindström[12], F. Linsel[11], J. Lipinski[13], B. List[11], P. Loch[27],
H. Lohmander[21], G.C. Lopez[20], V. Lubimov[23], D. Lüke[8,11], N. Magnussen[34],
E. Malinovski[24], S. Mani[7], R. Maraček[17], P. Marage[4], J. Marks[25], R. Marshall[22],
J. Martens[34], R. Martin[11], H.-U. Martyn[1], J. Martyniak[6], S. Masson[2], T. Mavroidis[20],
S.J. Maxfield[19], S.J. McMahon[19], A. Mehta[22], K. Meier[15], D. Mercer[22], T. Merz[11],
C.A. Meyer[37], H. Meyer[34], J. Meyer[11], S. Mikocki[6], D. Milstead[19], F. Moreau[28],
J.V. Morris[5], E. Mroczko[6], G. Müller[11], K. Müller[11], P. Murín[17], V. Nagovizin[23],
R. Nahnhauer[35], B. Naroska[13], Th. Naumann[35], P.R. Newman[3], D. Newton[18],
D. Neyret[29], H.K. Nguyen[29], T.C. Nicholls[3], F. Niebergall[13], C. Niebuhr[11], R. Nisius[1],

G. Nowak[6], G.W. Noyes[5], M. Nyberg-Werther[21], M. Oakden[19], H. Oberlack[26],
U. Obrock[8], J.E. Olsson[11], D. Ozerov[23], E. Panaro[11], A. Panitch[4], C. Pascaud[27],
G.D. Patel[19], E. Peppel[35], E. Perez[9], J.P. Phillips[22], Ch. Pichler[12], D. Pitzl[36], G. Pope[7],
S. Prell[11], R. Prosi[11], G. Rädel[11], F. Raupach[1], P. Reimer[30], S. Reinshagen[11],
P. Ribarics[26], H. Rick[8], V. Riech[12], J. Riedlberger[36], S. Riess[13], M. Rietz[2], E. Rizvi[20],
S.M. Robertson[3], P. Robmann[37], H.E. Roloff[35], R. Roosen[4], K. Rosenbauer[1],
A. Rostovtsev[23], F. Rouse[7], C. Royon[9], K. Rüter[26], S. Rusakov[24], K. Rybicki[6],
R. Rylko[20], N. Sahlmann[2], E. Sanchez[26], D.P.C. Sankey[5], M. Savitsky[23], P. Schacht[26],
S. Schiek[11], P. Schleper[14], W. von Schlippe[20], C. Schmidt[11], D. Schmidt[34], G. Schmidt[13],
A. Schöning[11], V. Schröder[11], E. Schuhmann[26], B. Schwab[14], A. Schwind[35],
U. Seehausen[13], F. Sefkow[11], M. Seidel[12], R. Sell[11], A. Semenov[23], V. Shekelyan[11],
I. Sheviakov[24], H. Shooshtari[26], L.N. Shtarkov[24], G. Siegmon[16], U. Siewert[16], Y. Sirois[28],
I.O. Skillicorn[10], P. Smirnov[24], J.R. Smith[7], V. Solochenko[23], Y. Soloviev[24],
J. Spiekermann[8], H. Spitzer[13], R. Starosta[1], M. Steenbock[13], P. Steffen[11], R. Steinberg[2],
B. Stella[32], K. Stephens[22], J. Stier[11], J. Stiewe[15], U. Stösslein[35], K. Stolze[35],
J. Strachota[30], U. Straumann[37], W. Struczinski[2], J.P. Sutton[3], S. Tapprogge[15],
R.E. Taylor[38,27], V. Tchernyshov[23], C. Thiebaux[28], G. Thompson[20], P. Truöl[37],
J. Turnau[6], J. Tutas[14], P. Uelkes[2], A. Usik[24], S. Valkár[31], A. Valkárová[31], C. Vallée[25],
P. Van Esch[4], P. Van Mechelen[4], A. Vartapetian[11,39], Y. Vazdik[24], M. Vecko[30],
P. Verrecchia[9], G. Villet[9], K. Wacker[8], A. Wagener[2], M. Wagener[33], I.W. Walker[18],
A. Walther[8], G. Weber[13], M. Weber[11], D. Wegener[8], A. Wegner[11], H.P. Wellisch[26],
L.R. West[3], S. Willard[7], M. Winde[35], G.-G. Winter[11], A.E. Wright[22], E. Wünsch[11],
N. Wulff[11], T.P. Yiou[29], J. Žáček[31], D. Zarbock[12], Z. Zhang[27], A. Zhokin[23],
M. Zimmer[11], W. Zimmermann[11], F. Zomer[27] and K. Zuber[15]

[1] *I. Physikalisches Institut der RWTH, Aachen, Germany[a]*
[2] *III. Physikalisches Institut der RWTH, Aachen, Germany[a]*
[3] *School of Physics and Space Research, University of Birmingham, Birmingham, UK[b]*
[4] *Inter-University Institute for High Energies ULB-VUB, Brussels; Universitaire Instelling Antwerpen, Wilrijk, Belgium[c]*
[5] *Rutherford Appleton Laboratory, Chilton, Didcot, UK[b]*
[6] *Institute for Nuclear Physics, Cracow, Poland[d]*
[7] *Physics Department and IIRPA, University of California, Davis, California, USA[e]*
[8] *Institut für Physik, Universität Dortmund, Dortmund, Germany[a]*
[9] *CEA, DSM/DAPNIA, CE-Saclay, Gif-sur-Yvette, France*
[10] *Department of Physics and Astronomy, University of Glasgow, Glasgow, UK[b]*
[11] *DESY, Hamburg, Germany[a]*
[12] *I. Institut für Experimentalphysik, Universität Hamburg, Hamburg, Germany[a]*
[13] *II. Institut für Experimentalphysik, Universität Hamburg, Hamburg, Germany[a]*
[14] *Physikalisches Institut, Universität Heidelberg, Heidelberg, Germany[a]*
[15] *Institut für Hochenergiephysik, Universität Heidelberg, Heidelberg, Germany[a]*
[16] *Institut für Reine und Angewandte Kernphysik, Universität Kiel, Kiel, Germany[a]*
[17] *Institute of Experimental Physics, Slovak Academy of Sciences, Košice, Slovak Republic[f]*
[18] *School of Physics and Materials, University of Lancaster, Lancaster, UK[b]*
[19] *Department of Physics, University of Liverpool, Liverpool, UK[b]*
[20] *Queen Mary and Westfield College, London, UK[b]*
[21] *Physics Department, University of Lund, Lund, Sweden[g]*
[22] *Physics Department, University of Manchester, Manchester, UK[b]*
[23] *Institute for Theoretical and Experimental Physics, Moscow, Russia*

[24] Lebedev Physical Institute, Moscow, Russia[f]

[25] CPPM, Université d'Aix-Marseille II, IN2P3-CNRS, Marseille, France

[26] Max-Planck-Institut für Physik, München, Germany[a]

[27] LAL, Université de Paris-Sud, IN2P3-CNRS, Orsay, France

[28] LPNHE, Ecole Polytechnique, IN2P3-CNRS, Palaiseau, France

[29] LPNHE, Universités Paris VI and VII, IN2P3-CNRS, Paris, France

[30] Institute of Physics, Czech Academy of Sciences, Praha, Czech Republic[f,h]

[31] Nuclear Center, Charles University, Praha, Czech Republic[f,h]

[32] INFN Roma and Dipartimento di Fisica, Universita "La Sapienza", Roma, Italy

[33] Paul Scherrer Institut, Villigen, Switzerland

[34] Fachbereich Physik, Bergische Universität Gesamthochschule Wuppertal, Wuppertal, Germany[a]

[35] DESY, Institut für Hochenergiephysik, Zeuthen, Germany[a]

[36] Institut für Teilchenphysik, ETH, Zürich, Switzerland[i]

[37] Physik-Institut der Universität Zürich, Zürich, Switzerland[i]

[38] Stanford Linear Accelerator Center, Stanford California, USA

[39] Visitor from Yerevan Phys.Inst., Armenia

1 Introduction

The measurement of the radiative elastic ($ep \rightarrow e\gamma + p$) and inelastic ($ep \rightarrow e\gamma + X$) scattering processes is of primary importance at HERA. Owing to the large centre of mass energy of the collisions, $\sqrt{s} = 296$ GeV, the above processes can be studied at HERA in a kinematic domain covering several orders of magnitude in q^2, the four-momentum squared carried by the exchanged virtual photon.

At low four-momentum transfer squared, $-q^2 \ll m_p^2$, where m_p is the proton mass, the elastic process dominates and, since the internal proton structure is unresolved, the corresponding cross section can be precisely calculated. This process is therefore used to monitor the luminosity at HERA [1, 2].

At large four-momentum transfer squared, $-q^2 \geq m_p^2$, the inelastic process dominates. In most deep inelastic lepton-nucleon scattering (DIS) experiments, at SLAC, the SPS and the Tevatron, the contribution of the inelastic radiative process ($\ell N \rightarrow \ell \gamma + X$) to inclusive DIS ($\ell N \rightarrow \ell + X$) was not resolved. This led to large radiative corrections to the measured nucleon structure functions. A fraction of these corrections arising from wide angle photon bremsstrahlung was experimentally verified by the EMC collaboration [3]. At HERA, efficient identification of radiative processes involving hard photon emission reduces the uncertainty of the radiative corrections [4, 5]. First results on the photon spectrum in radiative DIS have been given in [6, 7].

The emission of photons collinear with the incident electrons can be interpreted as a reduction of the effective electron beam energy. This effect can be exploited in order to probe the internal structure of the proton at distances larger than previously studied at HERA and to determine the cross sections for scattering of longitudinally, σ_L, and transversely, σ_T, polarized photons [8].

In the present paper we analyse the radiative processes observed in the H1 detector. Our primary goal is to discuss various methods of luminosity measurement, their uncertainties and the possibility of improvements in this domain. Another aim is to cross-check experimentally the size of radiative corrections to the DIS cross section at HERA. Finally, we present a study of a subsample of radiative DIS events with hard photons detected in the angular range of $\theta'_\gamma = \pi - \theta_\gamma \leq 0.45$ mrad. (Note that in the HERA convention used throughout this paper, the polar angles θ are measured with respect to the incoming proton direction, while the angles θ' are measured with respect to the incoming electron direction). It is our aim to provide first constraints on the proton structure functions at low Q^2.

The paper is organized as follows. The terminology and characteristics of radiative events are discussed in section 2. In sections 3 and 4 we describe the H1 detector and specify the selection criteria for the five radiative event samples which are used in the following sections. In section 5 we present four largely independent methods of luminosity measurement and discuss their systematic uncertainties. The spectrum of radiative photons originating from radiative deep inelastic scattering and measured in the angular range $\theta'_\gamma \leq 0.45$ mrad is compared with theoretical calculations in section 6. In section 7 we present the measurement of the differential cross section $d\sigma/dQ^2$ using the sample of radiative DIS events.

4

2   Radiative processes and their kinematics

2.1   Definitions

The dominant contributions to radiative elastic and inelastic scattering are those described by the diagrams shown in Fig. 1. The processes of real photon emission from the lines linked to the hadronic vertex can be neglected in the kinematic domain discussed in this paper.
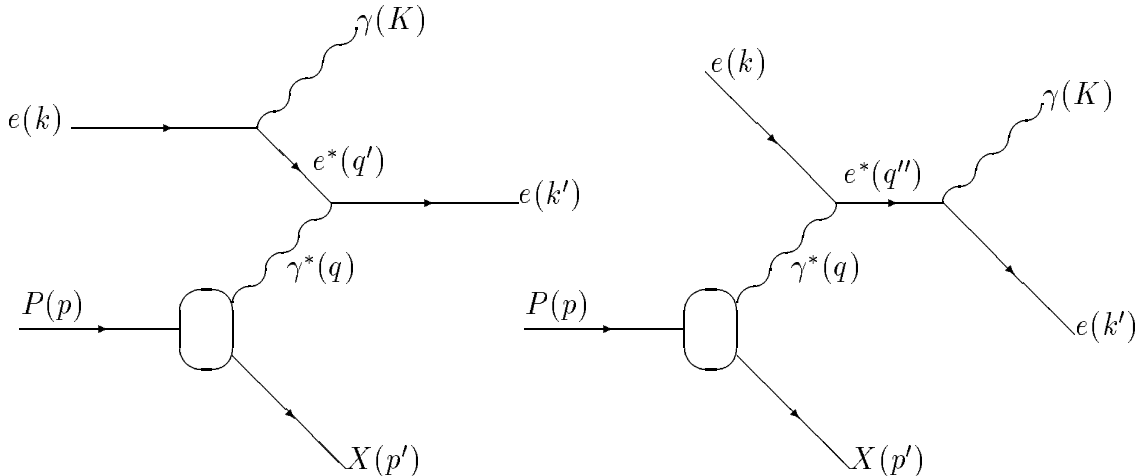
Figure 1: The diagrams for the radiative ($ep \to e\gamma + X$) scattering.

The kinematic variables, p, k, p', k' and K are, respectively, the four-vectors of the incident proton, incident electron, hadronic system (a proton in the elastic case), scattered electron and radiated photon. Five independent Lorentz-invariant variables describe the kinematics of radiative processes:

$$q^2 = (p' - p)^2 \tag{1}$$
$$s = (k + p)^2 \tag{2}$$
$$t = (K - k)^2 \tag{3}$$
$$W_{e\gamma}^2 = (k' + K)^2 \tag{4}$$
$$W^2 = p'^2 \ . \tag{5}$$

The four-momentum transfer squared, t, and $W_{e\gamma}^2$, the $e\gamma$ invariant mass squared, correspond to q'^2 and q''^2 in the diagrams in Fig 1.

The radiative scattering cross section is large in the neighbourhood of the poles of the virtual electron and virtual photon propagators. Following ref. [9] we define three classes of radiative processes corresponding to these kinematic domains:

- The **bremsstrahlung process** corresponding to the poles in both the virtual electron and the virtual photon propagators.

- The **QED Compton process** corresponding to the pole in the virtual photon propagator and to a large virtual electron mass.

- The **radiative DIS process** corresponding to the pole in the virtual electron propagator and to a large virtual photon mass.

In the H1 detector (see section 3 for more detailed detector description) the radiative photons are measured in two angular domains: ($\theta'_\gamma \leq \theta'_{pa} \simeq 0.45$ mrad) corresponding to the acceptance region of the photon arm of the luminosity detector and $\theta'_{cd1} \leq \theta'_\gamma \leq \theta'_{cd2}$, where $\theta'_{cd1} \simeq 0.07$ rad and $\theta'_{cd2} \simeq \pi - 0.05$ rad, corresponding to the acceptance region of the central detector. The scattered electrons are measured either in the central detector or in the electron arm of the luminosity detector, which detects electrons in the angular range $\theta'_e \leq \theta'_{ea} \simeq 5$ mrad. The produced hadrons are measured in the angular acceptance region of the central detector. A radiative photon and the scattered electron of energy $E'_e \geq 10$ GeV cannot be resolved in any region of the central detector if the photon emission angle, $\delta_{e\gamma}$, with respect to the electron is smaller than $\delta_{cd} \simeq 0.02$ rad.

In the following we discuss the experimental signatures of the three classes of radiative processes in the H1 detector in which $E_p = 820$ GeV protons interact with $E_e = 26.7$ GeV electrons. We shall define the way we separate these processes on the basis of their distinct experimental signatures.

2.2   The bremsstrahlung process

In the bremsstrahlung process the masses of the virtual photon and of the virtual electron are small: $0 \leq -q^2, -q'^2, q''^2 \lesssim (E_e\theta'_{pa})^2 \simeq 0.00015$ GeV^2. In this kinematic domain the elastic channel ($ep \rightarrow ep\gamma$) is the dominant process. The electron radiates a photon in the electromagnetic field of a proton, which can be regarded as point-like. Both the outgoing electron and the photon emerge at very small angles with respect to the incident electron direction ($\theta'_\gamma \lesssim \theta'_{pa}$ and $\theta'_e \lesssim \theta'_{ea}$). The recoil proton continues its motion almost undisturbed. Events of this type are identified either by detecting both the scattered electron and the photon, or by detecting only the photon. In the bremsstrahlung process the energy of the photon, E_γ, and the energy of the scattered electron, E', are constrained:

$$E_e = E'_e + E_\gamma \quad . \tag{6}$$

In the ultrarelativistic limit and in the small angle approximation the bremsstrahlung cross section is described by the Bethe-Heitler formula [10]. The effects related to the transverse and longitudinal beam sizes and densities [11, 12] can be safely neglected for the range of photon energies ($E_\gamma \geq 5$ GeV) discussed in this paper. Since the cross section is insensitive to the internal proton structure, the bremsstrahlung process can be used for luminosity measurement at ep colliders [2].

2.3   The QED Compton process

In the QED Compton process both $-q'^2$ and q''^2 are large, $-q'^2, q''^2 \gtrsim (E_e\theta'_{cd1})^2 \simeq 3.5$ GeV^2 (off-shell electron) and $-q^2$ is small, $m_p^2(W_{e\gamma}^4/s^2) \leq -q^2 \ll -q'^2, q''^2$ (quasi-real photon). Ignoring the hadronic vertex, this process corresponds to the Compton scattering of a quasi-real photon on an incident electron [1]:

$$e + \gamma^* \rightarrow e + \gamma \tag{7}$$

The dominant contribution to Compton scattering, which is sometimes called *wide angle bremsstrahlung* is due to the elastic channel ($ep \rightarrow ep\gamma$). Since the elastic form factor of the proton is well measured this process can also be used to measure the luminosity at

6

HERA. The inelastic contribution is no longer negligible with respect to the elastic one because the minimal $-q^2$ in the Compton process is significantly larger than the minimal $-q^2$ for the bremsstrahlung process ($W_{e\gamma} \gg m_e$). This contribution is, however, small and well known as long as $-q^2$ remains small.

The scattered electron and the photon are observed in the central detector ($\theta'_{e,\gamma} \geq \theta'_{cd1}$). As $-q^2$ is small, the proton (hadronic final state system) and the ($e - \gamma$) system have transverse momenta close to zero. The hadronic final state remains undetected in most of the cases ($\theta_{p,X} \leq \theta_{cd2}$).

Six kinematic variables describing the Compton process are measured in the H1 detector, namely the emission angles of the final state particles (θ_e, θ_γ) and (ϕ_e, ϕ_γ) and their energies E'_e and E_γ. Only three of these are independent if one neglects the hadronic (the ($e - \gamma$) system) transverse momentum. In this case the following three conditions constrain the kinematic variables of the Compton process:

$$\Delta\phi = \pi - |\phi_e - \phi_\gamma| \simeq 0 \ , \tag{8}$$

where $\Delta\phi$ is the acoplanarity angle, and

$$
\begin{aligned}
E'_e(\theta_e, \theta_\gamma) &= \frac{2E_e \sin\theta_\gamma}{\sin\theta_e + \sin\theta_\gamma - \sin(\theta_e + \theta_\gamma)} \\
E_\gamma(\theta_e, \theta_\gamma) &= \frac{2E_e \sin\theta_e}{\sin\theta_e + \sin\theta_\gamma - \sin(\theta_e + \theta_\gamma)} \ .
\end{aligned}
\tag{9}
$$

Note that in the Compton process the corrections of the order α^4 (second order radiative corrections) have to be taken into account, in particular the dominant one corresponding to hard photon emission in the direction of the incoming electron.

2.4 The radiative DIS process

In the radiative DIS process $-q^2$ is large, $-q^2 \gtrsim (E_e\theta'_{cd1})^2 \simeq 3.5$ GeV^2 (off-shell photon), while either $-q'^2$ or q''^2 is small, $-q'^2 \lesssim (E_e\theta'_{pa})^2 \simeq 0.00015$ GeV^2, $q''^2 \lesssim (E_e\delta_{cd})^2 \simeq 0.3$ GeV^2 (quasi-real electron). Since the elastic form factors of the proton decrease rapidly with increasing $-q^2$ and the inelastic structure functions rise, this process is dominated by the inelastic channel.

As $-q^2$ is large, the scattered electron or the ($e - \gamma$) system is observed in the angular range $\theta'_e \geq \theta'_{cd1}$ and a large fraction of the produced hadrons is detected. The transverse momentum of the hadronic system is balanced by the transverse momentum of the electron ($e - \gamma$ system). The angular distribution of radiated photons in DIS exhibits two peaks around the directions of the incident and of the scattered electron, corresponding to the regions of small $-q'^2$ and small q''^2 respectively.

Most of the radiative photons emitted in the direction of the scattered electrons of energy $E'_e \geq 10$ GeV can not be resolved in the H1 detector. However a sizeable fraction of events with radiative photons emitted in the direction of the incoming electrons can be identified in the H1 detector. These events may be interpreted as originating from non-radiative scattering at reduced electron beam energy [8]. The effective electron beam energy E_t is determined directly from the measured radiative photon energy E_γ:

$$E_t = E_e - E_\gamma, \tag{10}$$

and/or, as in [13], from the formula:

$$E_t = E_e \left(1 - (y_e - y_h) \right). \tag{11}$$

The inelasticity parameters y_e and y_h are expressed in terms of the energy, E'_e, and the angle, θ_e, of the scattered electron, and the momenta, p_h, and the angles θ_h, of all produced hadrons, according to the formulae:

$$y_e = 1 - \frac{E'_e}{E_e} \sin^2 \frac{\theta_e}{2} \tag{12}$$

and

$$y_h = \frac{\Sigma \left(E_h - p_h \cos \theta_h \right)}{2 \, E_e} \quad . \tag{13}$$

We describe ep collisions at reduced energy E_t using the "true" variables Bjorken-x_t, y_t and Q_t^2 defined as:

$$x_t = \frac{E_t \, E'_e \, \cos^2 \theta_e/2}{E_p \left(E_t - E_e \sin^2 \theta_e/2 \right)}, \tag{14}$$

$$y_t = 1 - \frac{E'_e}{E_t} \sin^2 \frac{\theta_e}{2}, \tag{15}$$

$$Q_t^2 = 4 \, E'_e \, E_t \cos^2 \theta_e/2, \tag{16}$$

where E_p denotes the energy of the proton beam. These formulae are obtained by replacing the nominal electron beam energy, E_e, by the effective electron beam energy, E_t, in the conventional expressions for x_e, y_e and Q_e^2, given e.g. in [6].

For the process of collinear emission of a radiative photon with respect to the incoming electron these variables describe directly the interaction of the virtual photon with the proton ($Q_t^2 = -q^2$).

3 The H1 detector

A detailed description of the H1 detector and its performance can be found in [14]. Below, we discuss a few aspects of the detector which are relevant for the measurement of the processes introduced in section 2.

Electrons and photons originating from bremsstrahlung processes are detected in the H1 luminosity system. This consists of a photon detector (PD) and water Čerenkov counter (VC), forming the photon arm, and an electron tagger (ET). A typical bremsstrahlung event is shown in Fig. 2.

Photons emitted collinearly with the incident electron direction leave the proton beam pipe through an exit window at $z = -92.3$ m where the pipe bends upwards, and hit the photon detector. This detector, situated at $z = -102.9$ m, is built out of 25 KRS-15 crystals [15] with a total surface of 100×100 mm^2 and a depth of 22 radiation lengths (X_0). A $2\,X_0$ long lead filter (F), followed by a $1\,X_0$ long water Čerenkov counter (VC), is located in front of the photon detector. The filter protects the photon detector against synchrotron radiation. The water Čerenkov counter serves primarily as a veto counter (to tag and reject early photon showers), but also provides a rough energy measurement, which is combined with the energy measurement in the crystals. The aperture of the

8

photon detector is $\theta'_{pa} \leq 0.45$ mrad, limited by the inner diameter of a lead collimator. This corresponds to an acceptance of ≈ 98 % for bremsstrahlung photons, which varies only slightly with changes of the beam optics.

Electrons emerging from the bremsstrahlung process are deflected by the HERA beam magnets in the region 5.8 m$< -z <$ 23.8 m, pass through an exit window at $z = -27.3$ m, and hit the electron tagger at $z = -33.4$ m. The latter, of the same type as the photon detector calorimeter, is made of 49 crystals, covering a total area of 154×154 mm^2. The acceptance of the electron tagger is defined by the fields in the machine magnets, and thus may vary significantly if the beam optics changes. The dependence of the tagger acceptance on the electron beam tilt and horizontal offset at the H1 interaction point (IP), as predicted by Monte Carlo simulation, is illustrated in Fig. 3. The actual value of the beam tilt is measured online with a precision of 0.01 mrad by reconstructing the average position of the photon spot in the PD. A possible offset of the electron trajectory at the IP cannot be directly monitored in the present detector configuration and therefore is not known online.

The measurement of the bremsstrahlung event rate within the acceptance of the luminosity detectors provides fast online monitoring of the luminosity. The H1 luminosity system trigger allows for several independent and dead time free scalers which can be used simultaneously. Thus, different methods of counting bremsstrahlung events can be
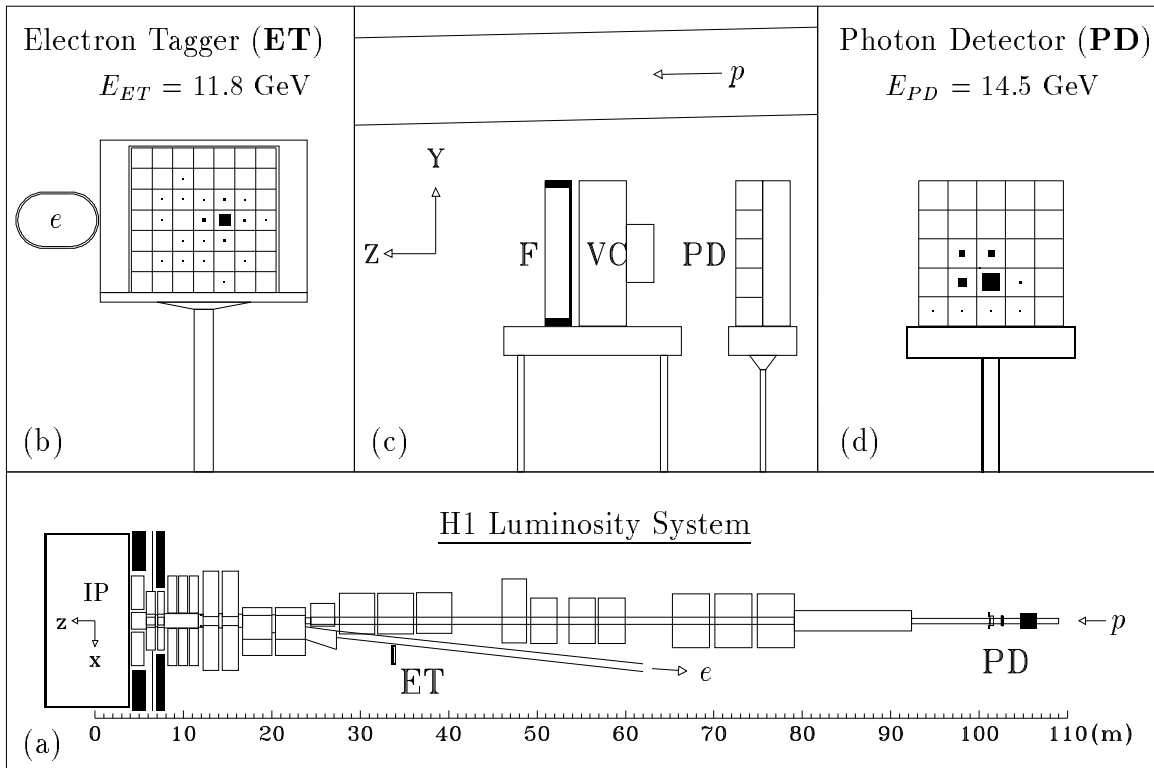
Figure 2: Example of a typical bremsstrahlung event detected in the H1 luminosity system: The top view of the H1 luminosity system is shown in the lower figure (a) where the location of the electron tagger (**ET**) and the photon detector (**PD**) can be seen with respect to the beam lines of e, p and the interaction point (IP). The electron tagger (b) is located directly beside the electron beampipe. A side view of the photon arm consisting of a filter (**F**), a water Čerenkov counter (**VC**) and the photon detector (**PD**) is shown in (c). The photon detector (d) is located in the median plane of the electron ring.

9
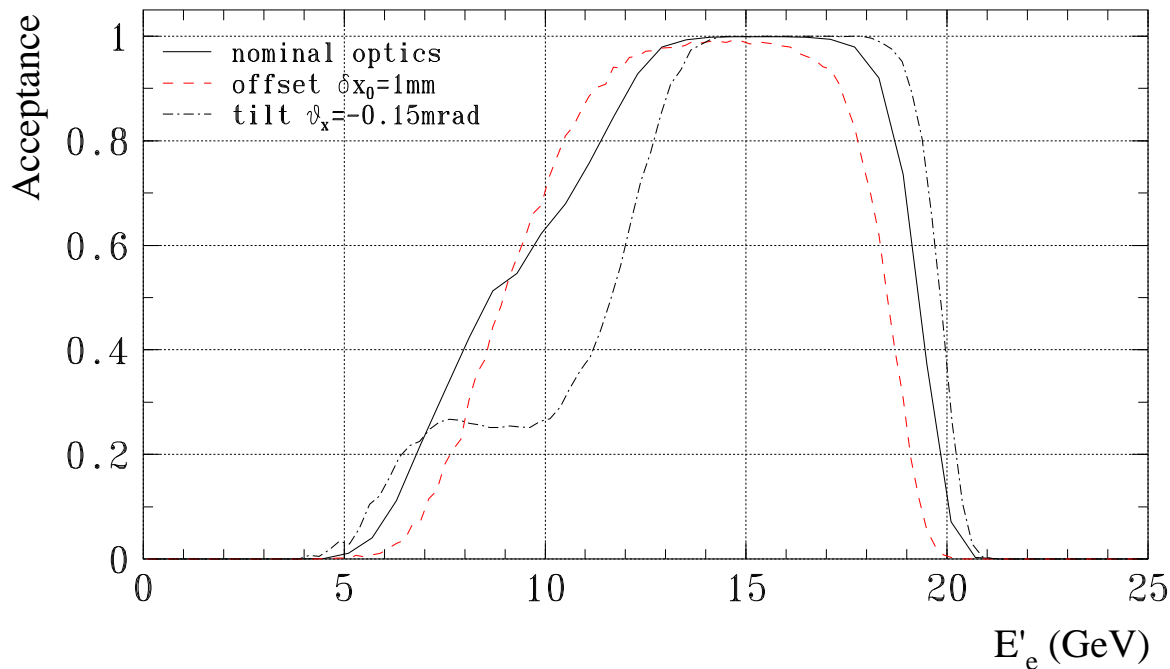
Figure 3: The simulated acceptance of the H1 electron tagger for different beam conditions. Full line: nominal optics (zero tilt and offset of the electron beam at the interaction point); dashed line: 1 mm offset of the electron beam in the horizontal direction, towards the centre of the HERA ring; dash-dotted line: -0.15 mrad horizontal tilt of the electron beam at the interaction point.

implemented online. A final absolute measurement of the integrated luminosity used for physics analysis requires a precise absolute energy calibration and detailed understanding of the acceptances of the luminosity detectors, and is performed offline. The absolute calibration of the luminosity system is continuously monitored during data taking and is discussed in section 4.1.

Electrons and photons originating from Compton processes are detected either in the backward electromagnetic calorimeter (BEMC) or in the liquid argon (LAr) calorimeter. A typical Compton scattering event is shown in Fig. 4.

The BEMC is made of 88 lead/scintillator sandwich stacks, each with a depth of 22 radiation lengths (X_0), corresponding to about 1 interaction length. It covers the angular range of $155^o < \theta_e < 176^o$. The stacks have transverse dimensions of 16×16 cm². Two pairs of 8 cm wavelength shifter bars with photodiode readout cover opposite sides of each stack. The absolute calibration of the BEMC stacks is determined from dedicated studies of deep inelastic scattering events (the kinematic peak method [16]). For events analysed in this paper the overall BEMC energy scale is verified using a sample of Compton scattering events as discussed in the following section.

Four planes of a proportional chamber (BPC) located in front of the BEMC measure the impact position of charged particles hitting the BEMC with a precision of 1.5 mm.

At angles θ smaller than 155°, particle energies are measured in the highly segmented LAr calorimeter [17]. This consists of an electromagnetic section with lead absorber and a hadronic section with stainless steel absorber. The depth of the electromagnetic section varies between 20 and 30 radiation lengths whereas the total depth of both sections varies between 4.5 and 8 interaction lengths. The calibration of the LAr calorimeter
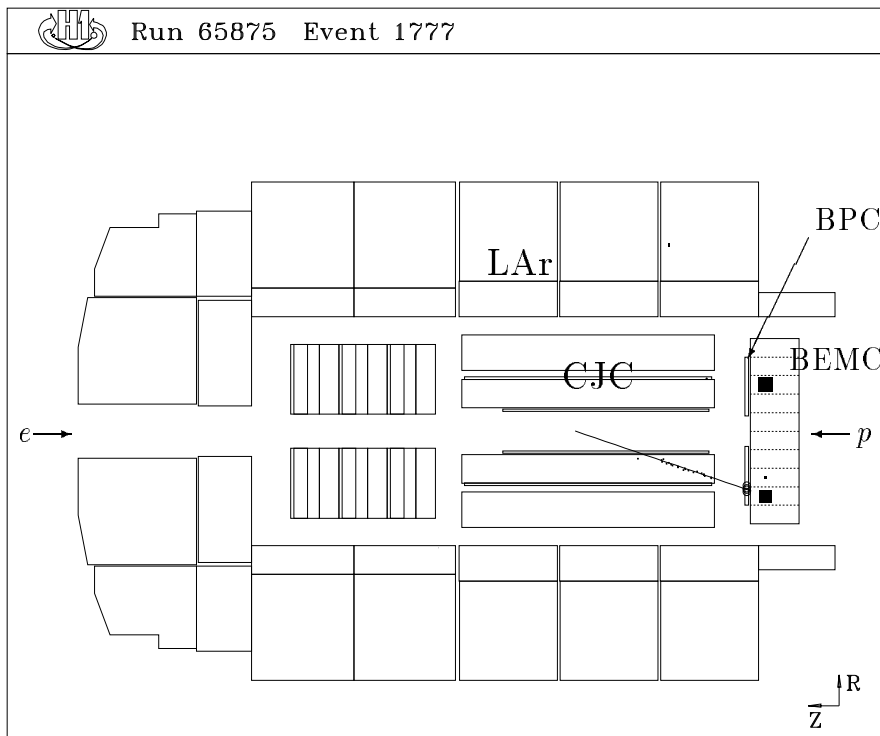
Figure 4: A QED Compton event in the H1 detector. The electron and photon are detected in the BEMC, the electron is also observed in the CJC and BPC whereas the photon produces no signals in these detectors.

segments has been obtained from test beam measurements using electrons and pions [14, 17, 18]. The electromagnetic energy scale has been verified to a 3 % accuracy in the H1 detector by comparing the measured track momentum of electrons and positrons with the corresponding energy deposit in the calorimeter cells and, at high electron energies, by exploiting the double angle method [16] for kinematic reconstruction of DIS events. The absolute scale of the hadronic energy is presently known to 6 % as determined from studies of the p_t balance of deep inelastic scattering events [16].

Charged particle tracks are measured in two concentric drift chamber modules (CJC) of angular acceptance $15° < \theta < 165°$ and in forward tracking detectors (FTD) covering smaller angles. A superconducting coil provides a uniform magnetic field of 1.15 T in the tracking region which allows the determination of charged particle momenta. In the majority of events analysed in this paper the electrons detected in the BEMC leave no track in the CJC due to the limited angular acceptance of these chambers. Therefore their angles (θ_e, ϕ_e) have to be determined in the same way as the angles of photons $(\theta_\gamma, \phi_\gamma)$, namely from the position of the reconstructed event vertex and the centre of gravity of the corresponding shower detected in the BEMC calorimeter. The vertex position is determined on an event by event basis, if one track reconstructed in the CJC or FTD crosses the beamline in the interaction region. If no such track is reconstructed the interaction vertex is assumed to be at its nominal z position. In the majority of radiative DIS events the vertex position is determined from charged hadron tracks as shown in Fig. 5.

The determination of y_h according to relation (13) uses combined calorimetric measurements and reconstructed charged tracks, avoiding double counting of energy [16].

11
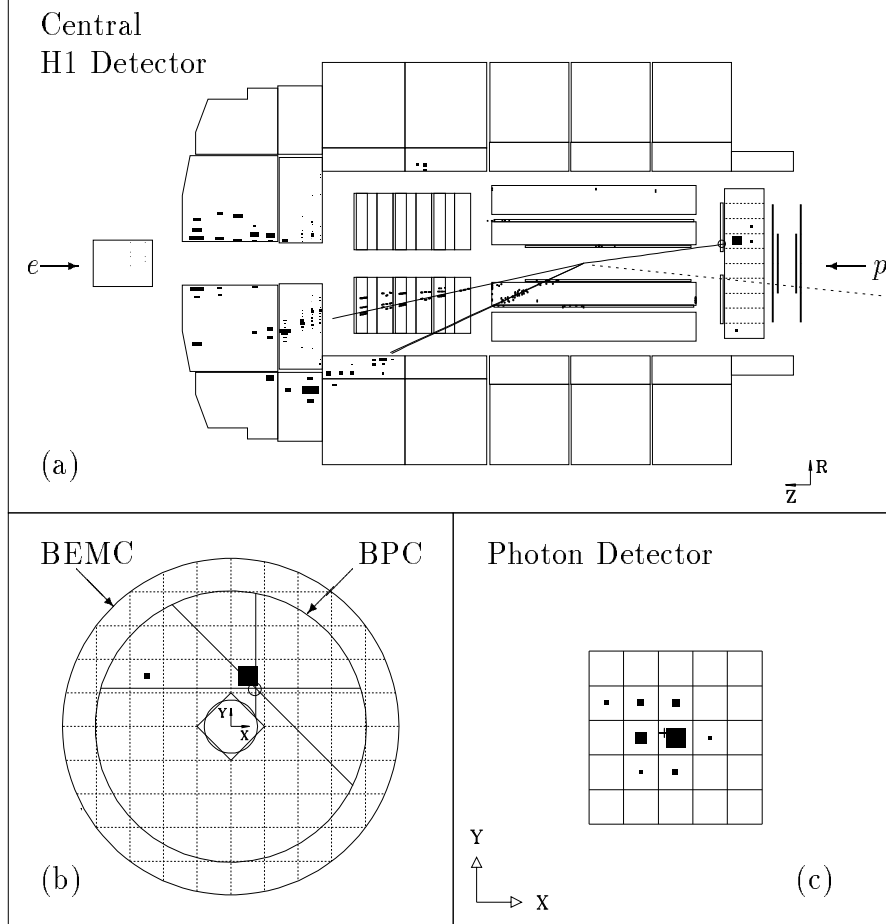
Figure 5: A radiative DIS event in the H1 detector. The scattered electron was detected in the BPC – indicated by the hit sense wires – and in the BEMC shown in (b). The particles of the hadronic final state were passing the central and forward tracking devices and were measured in the LAr calorimeter. The radiated photon was detected in the PD (c). The dotted line in (a) shows the expected direction of the quark jet for a non-radiative event with the same E'_e and θ_e.

4 Event selection and detector calibration

Three types of bremsstrahlung samples, a Compton event sample and a radiative DIS event sample were selected from the data accumulated by the H1 detector in the 1993 run period.

The rate of bremsstrahlung events observed in the H1 detector is very high ($\approx$ 15 kHz at the average 1993 luminosity). Typically, therefore, only a small proportion of these events are selected for analysis. Nonetheless the resulting statistical errors are much smaller than the systematic uncertainties which were already dominant at very low luminosity shortly after the comissioning of HERA. On the other hand the expected samples of Compton and of radiative DIS events are small. Here the statistical errors still dominate the systematic ones.

In 1993 HERA was operated with 84 colliding bunches at 96 ns intervals. In addition, 10 electron and 6 proton bunches (pilot bunches) had no partners allowing the level of beam gas background to be monitored.

4.1   The bremsstrahlung event samples

Three samples of bremsstrahlung events were selected. The $(e - \gamma)$ coincidence sample, the hard γ sample and the random sample. The selection criteria used are discussed below.

Events belonging to the $(e - \gamma)$ **coincidence sample** were required to have coincident energy deposits in the photon arm, $E_\gamma = E_{PD} + E_{VC}$, ($E_{PD}$ and E_{VC} are correspondingly the energy deposits in the photon detector and the water Čerenkov counter) and in the electron tagger, E_{ET}. These deposits were required to satisfy the following conditions:

- $E_{ET} \geq 5$ GeV,

- $E_\gamma \geq 5$ GeV,

- 23 GeV $\leq E_{ET} + E_\gamma \leq 30$ GeV,

- $|x_{ET}| \leq 65$ mm and $|y_{ET}| \leq 65$ mm.

The last condition, where x_{ET} and y_{ET} are the coordinates of the electron impact point with respect to the centre of the electron tagger, was used to reject events in which a large amount of energy leaks over the transverse detector boundaries, which is essential only for the electron tagger. This sample was used for the offline energy calibration of the luminosity system. The crystal calorimeters were calibrated with events having $E_{VC} < 0.2$ GeV, while the water Čerenkov counter was calibrated with those having $E_{VC} > 0.2$ GeV.

The first three requirements were also implemented in the dead time free luminosity system trigger, which provides the online monitoring of the instantaneous luminosity variations and fast estimation of the luminosity. To a large extent this measurement is independent of time variations of the trigger thresholds and of the precise understanding of the time dependent energy calibration of the detectors. On the other hand, as we mentioned in the previous section, it depends strongly upon the beam optics, and therefore has to be cross-checked offline by another method, insensitive to such effects.

To cross-check the results of the above luminosity measurement the **hard γ sample** was used. The events belonging to this sample selected using only the photon arm, were required to have a reconstructed photon energy $E_\gamma \geq 10$ GeV. The main advantage of this event sample over the previous one is that its selection efficiency is insensitive to possible time dependent variations of the beam optics. On the other hand, it requires a precise knowledge of the absolute calibration and resolution of the photon detector.

The selection criteria for the two event samples described above were based solely on the quantities measured in the luminosity system. These events were triggered, read out and analysed on a stand alone basis, i.e. independent of the status of the central detector. The third sample, on the contrary, contains bremsstrahlung events which happened to occur in the same bunch crossing as another electron proton interaction which triggered the readout of the full H1 detector. This **random sample** was selected using the following criteria:

1. $E_\gamma \geq 5$ GeV,

2. An electromagnetic cluster was reconstructed in the BEMC with $E'_e \geq 25$ GeV. This requirement rejects all radiative DIS events with a photon of $E_\gamma \geq 5$ GeV emitted in the acceptance region of the photon arm.

This event sample is small (170 events). The bremsstrahlung events were registered independently of the electron tagger and photon arm triggers, providing a cross-check of their efficiencies.

All three event samples described above contain background events. These are mainly due to bremsstrahlung on the residual gas in the beam pipe. The contribution of such a background is changing with time and on average amounts to ≈ 30 % for the 1993 run period. It can be monitored using a sample of bremsstrahlung events associated with electron pilot bunches and statistically subtracted. The accuracy of the statistical subtraction is discussed in section 5.

The absolute calibration of the sum of energies ($E_\gamma + E_{ET}$) is determined with a precision better than 1 % using the energy constraint (6) discussed in section 2.2. This is illustrated in Fig. 6 where the correlation of E_γ vs. E_{ET} and the distribution of $E_\gamma + E_{ET}$ are shown for the coincidence sample. Note that the calibration of the total visible energy of the bremsstrahlung events is determined directly from the data and does not require a precise knowledge of the electron tagger acceptance. The relative calibration of E_γ and E_{ET} is determined with a precision of 1.3 % from studies of the E_γ and E_{VC} dependence of the mean $E_\gamma + E_{ET}$. Relative miscalibration of more than 1.3 % between the electron and the photon arms would lead to an observable tilt of the mean $E_\gamma + E_{ET}$ distribution as a function of E_γ.
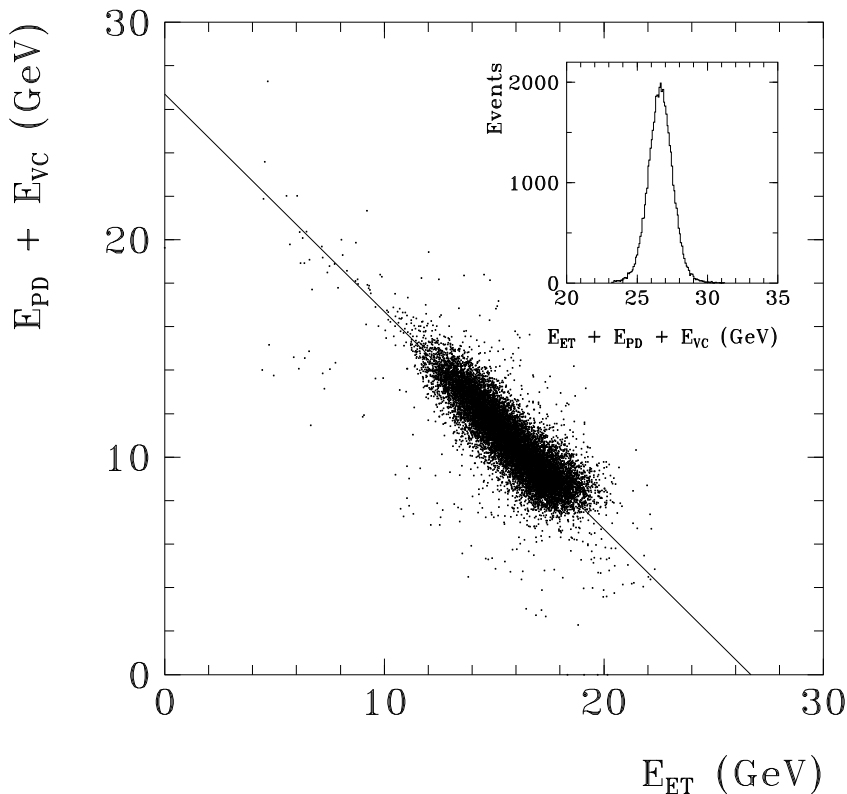
Figure 6: The correlation of the reconstructed electron energies (E_{ET}) and photon energies ($E_\gamma = E_{PD} + E_{VC}$), for the bremsstrahlung event sample. The corresponding distribution of $E_\gamma + E_{ET}$ is shown in the right upper corner.

14

In addition the absolute energy scale of the photon detector is determined using the high energy edge of the E_γ spectrum (Fig. 7) with a precision of better than 1 %. Taking into account a maximum nonlinearity of 1.3 % in the response of the photon arm the global energy scale is known with a precision of 1.5 % for $E_\gamma > 5$ GeV.

The resolution function of E_γ was determined from the measured tail of the reconstructed photon energies with $E_\gamma \gtrsim E_e$. This tail is due both to the finite detector resolution and to the overlap of two bremsstrahlung events occuring in the same bunch crossing. To resolve the two contributions we assumed a gaussian shape of the E_γ resolution function, verified by studies of the coincidence sample. In Fig. 7 we show the measured energy spectrum of bremsstrahlung photons and compare it with the Monte Carlo spectrum simulated using the Bethe-Heitler formula [10]. The Monte Carlo includes event selection efficiency, E_γ resolution effects and pileup effects. The data and the theoretical predictions are seen to be in good agreement providing an independent cross-check of our understanding of the energy calibration of the luminosity detector.
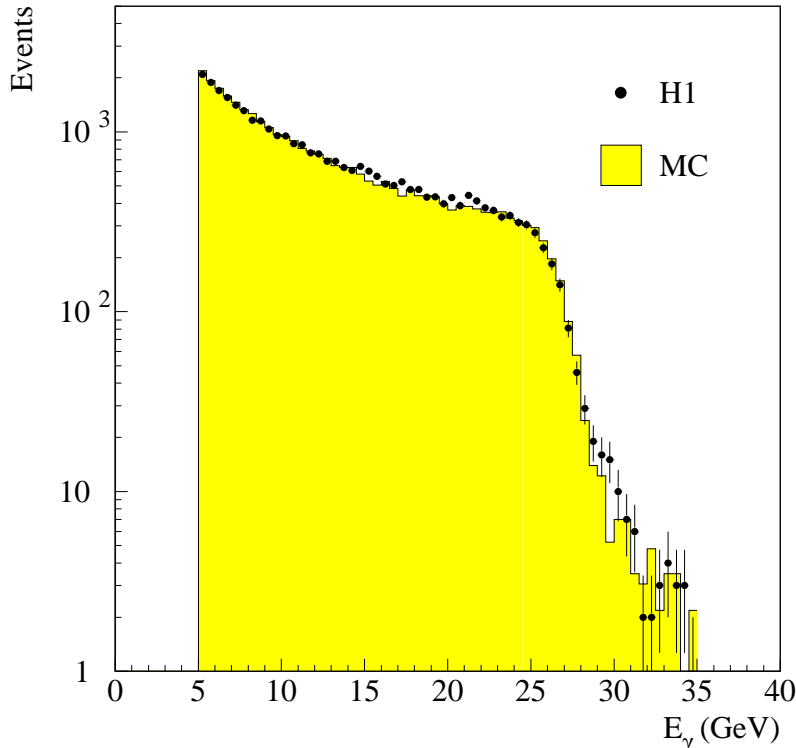
Figure 7: The E_γ spectrum for the bremsstrahlung process. The points represent the H1 data and the shaded area the Monte Carlo predictions based on the Bethe-Heitler formula.

4.2   The QED Compton event sample

The QED Compton event sample was selected by demanding the presence of two localized energy deposits (clusters) in the electromagnetic calorimeters of the central detector, corresponding to the final state electron and photon, explicitly demanding that no hadrons are detected. The deposits were required to satisfy the following conditions:

- the energy of one cluster: $E_{cl1} \geq 8$ GeV,

- the energy for the other cluster: $E_{cl2} \geq 2$ GeV,

15

- the total energy of the two clusters: $E_{vis} \geq 18$ GeV,

- the energy of any additional cluster: $E_{cl3} \leq 2$ GeV,

- the acoplanarity angle between the centres of gravity of the first two selected clusters $\Delta\phi < 45^\circ$.

In order to reject the remaining photoproduction background events we use the kinematic constraint defined in section 2.3 and restrict the selection to electromagnetic clusters. We define an estimator ξ^2:

$$\xi^2 = \sum_{i=1}^{2} \left(\frac{R_{cli} - <R_{cl}>}{\sigma_R} \right)^2 + \left(\frac{E_{cli}^{meas} - E_{cli}(\theta_{cl1}, \theta_{cl2})}{\sigma_E} \right)^2 , \qquad (17)$$

where R_{cli} is the transverse size of the energy cluster i as defined in [19], $<R_{cl}>$ is the corresponding average value for electromagnetic clusters, E_{cli}^{meas} is the measured cluster energy and $E_{cli}(\theta_{cl1}, \theta_{cl2})$ the energy calculated using equation (9). The errors σ_R and σ_E are derived from the data [19]. In the limit of the small transverse momentum of the $(e - \gamma)$ system, $p_\perp^{e\gamma} \to 0$, and neglecting radiative processes of order α^4 or higher, ξ^2 is equivalent to χ^2. We required the $\xi^2 < 14$.

The cross section for the Compton process is proportional to $dW_{e\gamma}/W_{e\gamma}^3$ [9]. The majority of events thus have a relatively small $(e - \gamma)$ invariant mass, leading to a small quasi real photon energy and to a boost of the $(e - \gamma)$ system in the direction of the incident electron (towards the BEMC).

In the selected sample of 338 events, 263 events have both the electron and photon detected in the BEMC and 70 events have one of the two final state particles in the BEMC and the other in the liquid argon calorimeter. The remaining 5 events with relatively high $(e - \gamma)$ invariant masses, up to 50 GeV, have both electron and photon detected in the liquid argon calorimeter.

The constraints relating the electron and the photon energies measured in the calorimeters (mostly the BEMC) to those derived from angles (equations 9) enable us to calibrate the absolute energy scale of the BEMC calorimeter with a precision better than 1 % and its transverse position to 1 mm [19]. The obtained energy scale is averaged over time and integrated over the fiducial volume of the BEMC. In addition, the QED Compton events allow us to cross-check the linearity of the BEMC response. It should be stressed that the calibration of the energy scale of the BEMC, including the effects of the dead material in front of it, is obtained directly from the ep scattering data and, except for the estimation of the residual radiative corrections to the Compton process, does not rely on a Monte Carlo simulation.

Fig. 8 shows the distributions of the three variables characterizing the Compton event sample: the invariant mass of the $(e - \gamma)$ system (for high masses this distribution has already been presented in [20]), the visible energy $(E_e' + E_\gamma)$ and the acoplanarity angle. These distributions are compared to the theoretical predictions. The latter are calculated using the COMPTON 2.0 event generator [9], which includes α^4 radiative processes, followed by a detailed simulation of the detector response and event reconstruction procedures identical to those used in the data reconstruction. The agreement observed between data (dots) and Monte Carlo predictions (histogram) indicates an adequate understanding and control of both the experimental data and the theoretical predictions.

16
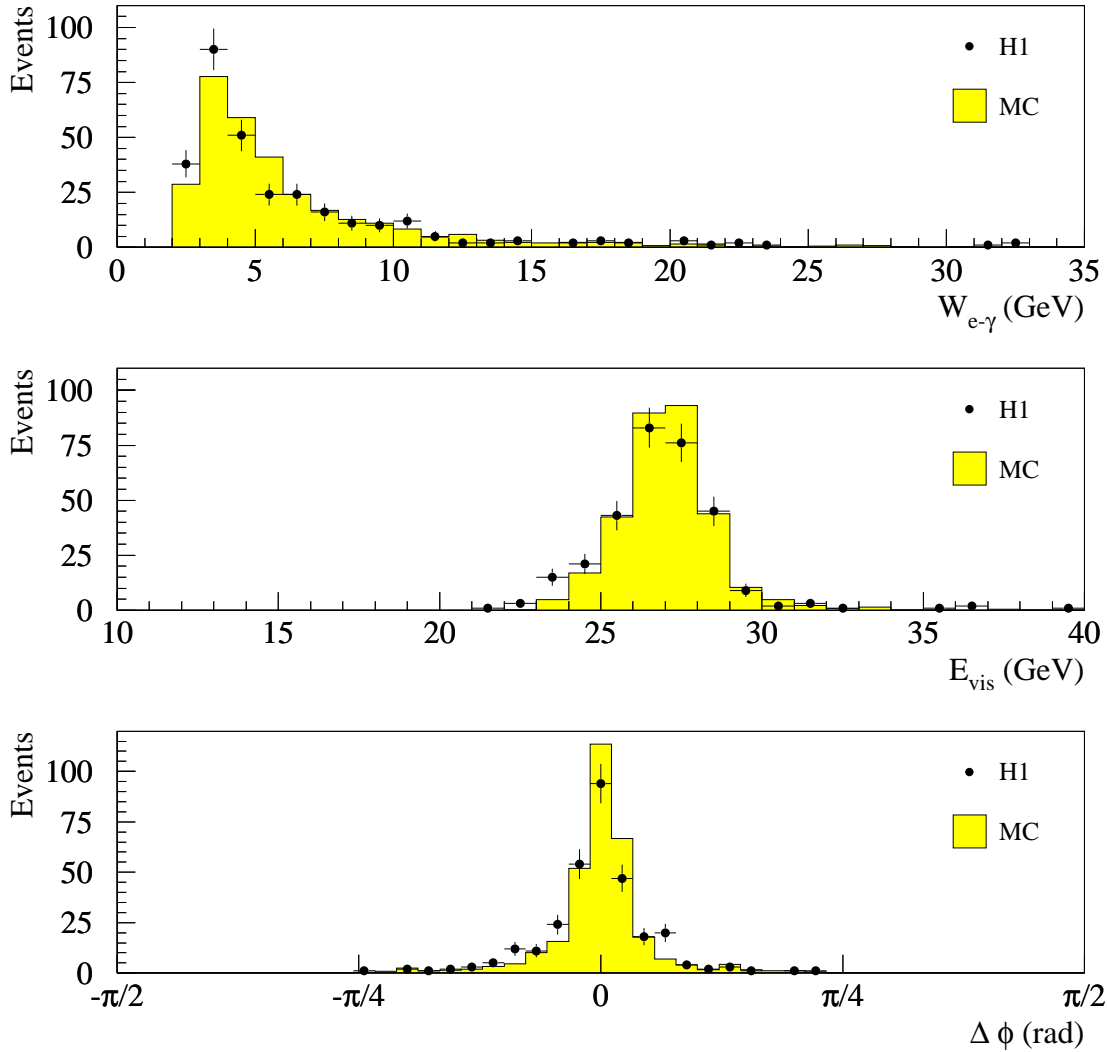
Figure 8: The distributions of: the mass of the $(e - \gamma)$ system, $W_{e\gamma}$; the visible energy, $E_{vis} = E'_e + E_\gamma$; the acoplanarity angle, $\Delta\phi$; for the Compton event sample. The points represent the H1 data. The shaded areas are the Monte Carlo predictions obtained using the COMPTON 2.0 generator normalized to the same number of events.

4.3 The radiative DIS event sample

Candidates for deep inelastic radiative scattering were selected according to the following criteria:

1. A BEMC energy cluster associated to a space point in the BPC was required. The cluster had to lie within $160° \leq \theta_e \leq 172°$ and had to have an energy $E_{clust} \geq 10$ GeV. The transverse separation of the cluster centre of gravity and the BPC space point was required to be smaller than 5 cm.

2. An event vertex, reconstructed from tracks in the central tracker, was required within $\pm$ 50 cm of the nominal interaction point along the z axis.

3. An electromagnetic energy cluster of energy larger than 5 GeV in the photon detector was demanded.

4. The energy deposited in the electron tagger was required to be less than 1 GeV.

The selected sample of 330 events contains both radiative DIS events and events in which non-radiative scattering occurs in the same bunch crossing as a bremsstrahlung event. These latter will be called hereafter pileup events. They are partly removed from the sample by requirement 4, but a sizeable fraction of them remains and this has to be subtracted statistically. The majority of these background events has the bremsstrahlung electrons outside the acceptance region of the electron tagger.

To estimate the pileup event background we use the redundancy of the effective electron beam energy measurement (equations (10) and (11) discussed in section 2). For radiative DIS events we expect the quantity Δ defined as:

$$\Delta = (E_\gamma - E_e(y_e - y_h))/E_\gamma \qquad (18)$$

to be concentrated around zero. For pileup events we expect Δ to be significantly different from zero. In particular, for pileup of bremsstrahlung and non-radiative DIS events we expect $y_e = y_h$, and the $\Delta \approx 1$.
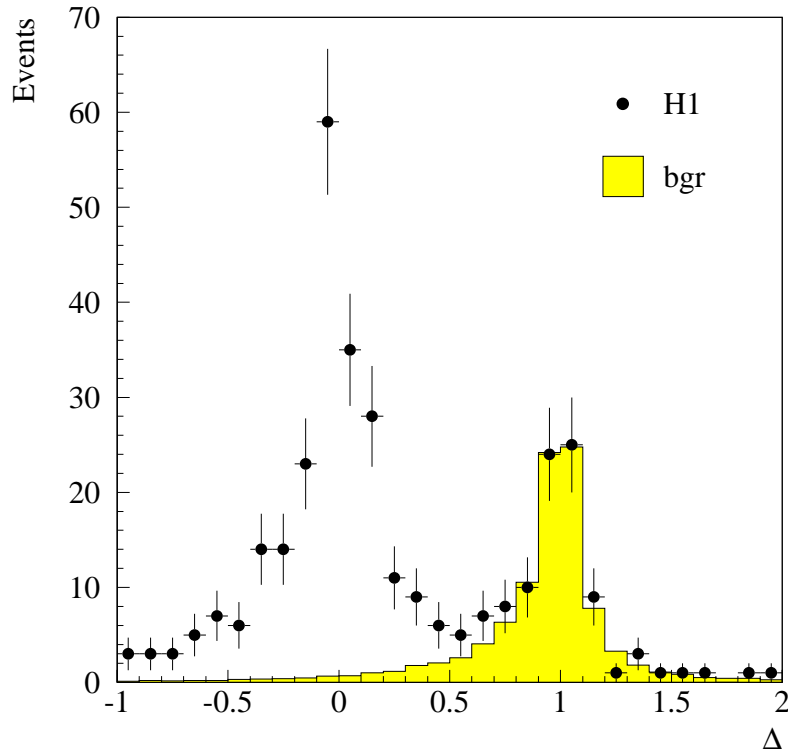
Figure 9: The distribution of $\Delta = (E_\gamma - E_e(y_e - y_h))/E_\gamma$ for the radiative DIS candidates. Only statistical errors are shown. The shaded area represents the background due to pileup events (see text for details).

In Fig. 9 the distribution of Δ is shown for the selected event sample. As expected, two peaks, at $\Delta = 0$ and $\Delta = 1$, are observed. In order to estimate the contribution of the pileup events as a function of Δ we randomly mixed events satisfying requirements 1 and 2 with the bremsstrahlung events. The Δ distribution for this artificial event sample was then normalized to the corresponding distribution of the radiative DIS candidates in the region $\Delta \geq 0.8$ where the radiative events do not contribute. The good agreement between the shapes of both spectra above $\Delta = 0.8$ strongly suggests the dominant contribution to the background is indeed pileup events. We therefore used the shape of the Δ distribution corresponding to the artificial event sample to estimate the remaining background for $\Delta \leq 0.8$.

18

5 Luminosity measurement

5.1 The $(e - \gamma)$ coincidence and the hard γ rate methods

In this section we present two methods of luminosity measurements based on the $(e - \gamma)$ coincidence and the hard γ bremsstrahlung event samples. The $(e-\gamma)$ coincidence method, which is insensitive to the observed rate dependent variations of the gain factors in the luminosity detectors, provides the online measurement in H1. The γ rate method, based on the hard γ sample selected according to the criteria specified in section 4.1, gives the most accurate offline value for the integrated luminosity after precise final calibration of the photon arm.

In both cases the average luminosity is calculated from the following relation:

$$L = \frac{N_{data}(\Delta t) - N_{bgr}(\Delta t)}{\sigma_{BH}^{acc} \, \Delta t}, \tag{19}$$

where $N_{data}(\Delta t)$ is the number of events satisfying the selection criteria for the given method collected in the time interval Δt and $N_{bgr}(\Delta t)$ is the number of background events originating from the interactions of electrons with residual gas in the beam pipe. This number is measured using the pilot bunches using the formula:

$$N_{bgr}(\Delta t) = \frac{I_{all}}{I_{pilot}} \, N_{pilot}(\Delta t) \,, \tag{20}$$

where N_{pilot} is the number of accepted bremsstrahlung events originating from the pilot bunches, I_{pilot} is the current of these bunches and I_{all} is the total electron current. The acceptance corrected value of the cross section for bremsstrahlung events σ_{BH}^{acc} is calculated using the Bethe-Heitler formula [10]. The relation (20) is based on the assumption that the pilot and colliding electron bunches are equivalent in terms of the background rate per unit of current (i.e. the background originates predominantly from beam gas bremsstrahlung while the beam wall contribution can be neglected). This assumption was checked by separating the electron and proton beams in several luminosity runs and was verified with an accuracy of better than 1 % (0.3 % in 1994). The precision of the background subtraction procedure in (19) using the estimate (20) depends on the error of the relative current measurement $(\delta(I_{all}/I_{pilot}) \lesssim 1 \text{ %})$, on the vacuum in the beam pipe and on the number of pilot bunches. For the 1993 running conditions this gave 0.9 % per 10 second online measurement cycle, and 1.5 % for the selected offline samples, reflecting the available statistics.

The major contribution to the systematic error in (19) comes from the determination of the acceptance corrected cross section σ_{BH}^{acc}. In the hard γ rate method this correction includes the effects of energy smearing in both the photon detector and the water Čerenkov counter and residual losses of events due to trigger inefficiency. The acceptance correction for the $(e - \gamma)$ coincidence method depends upon the optics of the electron beam and requires precise knowledge of the electron trajectory in the magnetic fields of HERA up to the entry to the electron tagger. An overall normalization error of up to 10 % is possible in extreme cases of large variations of the beam orbits. One has to stress that this problem concerns only the online measurements. Offline the electron tagger acceptance can be determined from the data, using the hard γ sample which contains $\approx$ 40 % of $(e - \gamma)$ coincidence events. Such a procedure was used to verify the energy and

time dependence of the integrated electron tagger acceptance function with a precision of $\approx$ 3 % and to correct the overall normalization used in the online measurement.

The dominant contributions to the systematic error of the absolute luminosity measurement in the $(e - \gamma)$ coincidence method are:

- Acceptance determination. In the online monitoring, where only the electron beam tilt is measured and can be accounted for, the overall error can be large. This is predominantly related to possible changes in the horizontal offset of the electron orbit at the IP. Other sources, such as the precision of the ET position and accuracy of the beam tilt measurement, are known at the level of $\approx$ 1 %, or better. Offline, the actual acceptance of the electron tagger is determined from the data with a precision of $\approx$ 3 % which is mainly defined by the absolute energy calibration of the luminosity system. No significant changes in the electron tagger acceptance were observed during the 1993 run period. Thus the corresponding uncertainty of 3 % was assigned to the online measurements as well.

- Background subtraction. This contribution is less than 1 % in the online, and $\approx$ 1.5 % for the offline sample, as discussed above.

- Trigger efficiency and purity. Both the online and offline errors from this source are small ($\approx$ 1 %) because the minimal energies required are well above the thresholds for both ET and PD.

In total the corresponding uncertainty of the measured instantaneous luminosity with the $(e - \gamma)$ coincidence method in 1993 was estimated to be 4 %.

The dominant contributions to the systematic error of the luminosity measurement using the hard γ rate method are:

- Absolute energy calibration and resolution of the γ-arm. 1.5 % precision of the photon arm energy calibration, together with the energy smearing due to the finite resolution, translates to $\approx$ 1.7 % uncertainty in σ_{BH}^{acc} for $E_\gamma \geq 10$ GeV.

- Trigger efficiency and purity. The corresponding error was estimated from several independently triggered samples having hard photons in the photon arm, and was found to be $\approx$ 2 %.

- Background subtraction and effect of multiple photons. The probability of having more than one energetic photon ($E_\gamma > 0.3$ GeV) in the same bunch crossing, which may in principle change the shape of the reconstructed energy spectrum in the photon detector, was small in 1993. The effect is visible for the high energy tail, $E_\gamma > E_e$, but the corresponding correction (0.2 ± 0.2 %) is neglected in the analysis. The error of the background subtraction using equation (20) is 1.5 %.

In total the corresponding uncertainty in the measured integrated luminosity with the hard γ rate method in 1993 is 3.4 %.

5.2 The random coincidence method

The integrated luminosity can also be derived from the random event sample selected according to the criteria described in section 4.1.

We determine first the average conditional probability P_{DIS-B} that a bremsstrahlung event satisfying requirement 1 ($E_\gamma \geq 5$ GeV) of the selection criteria for the random coincidence sample happen to occur in the same bunch crossing as a DIS event satisfying requirement 2 ($E_e' \geq 25$ GeV). This probability is given by $P_{DIS-B} = N_{1,2}/N_2$, where $N_{1,2}$ is the number of random coincidences satisfying both criteria 1 and 2, and N_2 is the number of events fulfilling the condition 2. If the luminosity were constant over a given running period then P_{DIS-B} would be equal to the probability P_{BC-B}, of registering a bremsstrahlung event in any randomly chosen bunch crossing. In reality the instantaneous luminosity varies with each electron and proton fill of the HERA storage rings and is unevenly distributed over 84 colliding bunches. Therefore, $P_{BC-B} = (1 - \kappa) P_{DIS-B}$ where κ is an average correction for the time variation of the instantaneous luminosity. This correction was determined using the time variation of the ($e - \gamma$) coincidence rate and was found to be (5 ± 1) % [21]. Note, that this correction is insensitive to both the absolute calibration of the luminosity system and the selection criteria for bremsstrahlung events.

Having determined P_{BC-B} we calculate the total number of bremsstrahlung events fulfilling requirement 1 as: $N_{BC-B}(\Delta t) = P_{BC-B} \times N_{bunch}(\Delta t)$, where $N_{bunch}(\Delta t)$ is the integrated number of bunch crossings over the time interval Δt. The corresponding luminosity is then calculated using formula (19) by replacing $N_{data}(\Delta t)$ by $N_{BC-B}(\Delta t)$.

The resulting integrated luminosity is independent of the efficiency of the photon detector trigger. Thus, the systematic errors for this method come from the same sources as for the hard γ method except that there is no error due to uncertainties in the trigger efficiency but an additional 1 % error due to κ. This results in a total systematic error of 2.8 % and a measurement error that is dominated by the statistical precision.

5.3 The Compton method

In the Compton method the luminosity is calculated from the following formula:

$$L = (\frac{N}{N' \, \epsilon_{sel}}) \, L' \quad , \tag{21}$$

where N is the number of events in the Compton event sample selected according to the criteria given in section 4.2, N' is the number of simulated events passing the same event selection criteria, L' is the luminosity corresponding to the simulated event sample. The ϵ_{sel} is introduced to take into account differences between Monte Carlo and data selection efficiencies and was determined directly from the data using the monitoring data samples.

The events from the Monte Carlo and the data samples are reconstructed and analysed with the same program. We have checked that the ratios of distributions of the kinematic variables in the data and Monte Carlo are independent of the ξ^2 cut defined in section 4.2 as long as $\xi^2 \leq \xi_0^2 = 14$. This indicates a very good agreement of the data and the Monte Carlo samples. Above $\xi^2 = 14$, the increasing background contribution present in the data, but not in the MC, causes visible distortions of the data/MC ratios.

The following systematic error sources dominate the overall error of this method:

- The selection efficiency. The cut on the energy of the third cluster (see section 4.2) introduces selection inefficiencies if artificial calorimetric electronic noise clusters remain in events with an otherwise acceptable Compton signal. This efficiency and its error was estimated to be (88.8 ± 3.5) % using the monitoring sample of events in which this requirement was dropped.

- The theoretical uncertainties in the Monte Carlo. The theoretical error on the cross section, related to the uncertainty in the elastic proton form factor, is ≈ 1 % if we select events with $q^2 \simeq p_T^2 \ll W_{e\gamma}^2$ using a very stringent cut on $\Delta\phi$. Such a cut requires a precise understanding of the resolution of the acoplanarity angle measurement. We use, at present, a weak $|\Delta\phi| \leq 45^o$ cut, which accepts some inelastic events. Their contribution is controlled using the observed tail of the $\Delta\phi$ distribution (Fig. 8) with precision of 3 %.

The interaction vertex is not reconstructed in the majority of the Compton events due to the small $W_{e\gamma}$. For these events the vertex is assumed to be at the run dependent nominal position. The uncertainties of the geometrical acceptance due to the time dependent variations of the position of the bunch crossing point as well as due to variations of the proton bunch size were found to be negligible.

The luminosity measured using the Compton method provides an important cross-check of the three methods discussed above. It is based solely on the measurements in the central detector. No additional corrections for data acquisition dead time and detector inefficiency are required.

5.4   Comparison of the methods

In order to represent the luminosity delivered in the acceptance region of the central detector, all luminosity values have to be further corrected for the effect of so called satellite bunches at HERA.

A fraction up to ≈ 10 % of the proton current may escape from the proton buckets during the preaccelerating and injection phase and form parasitic satellites distributed between the main proton bunches at distances which are integer multiples of $\pm$ 4.8 ns. Thus a fraction of the total integrated luminosity, originating from the satellite bunches colliding in the straight section of HERA ($\pm$ 6 m around the interaction point) and contributing to the luminosity measurement, but outside the fiducial volume of the main detector, must be corrected for.

The fraction of the luminosity originating from satellite bunches was estimated from an analysis of the ep vertex distributions using unbiased samples of photoproduction and low Q^2 DIS events (for the bremsstrahlung methods) and directly from the subsample of Compton events in which the interaction vertex is reconstructed (for the Compton method). The corresponding satellite bunch corrections, which may be different for the Compton method and for the three bremsstrahlung methods, were found to be (3.6 ± 2.5) % and $(3.3 \, {}^{+ \, 3.0}_{- \, 0.8})$ % respectively.

The four methods of the luminosity measurement discussed above have different sensitivity to the detector data acquisition dead time. In contrast to the measurement with the Compton events the three luminosity measurements which are based on the bremsstrahlung event samples have to be dead time corrected. This correction is made

Method	Stat. error	Syst. error	Sat. corr. error
$(e - \gamma)$ coincidence	negligible	4.0 %	$-3.0 + 0.8$ %
hard γ rate	0.6 %	3.4 %	$-3.0 + 0.8$ %
random coincidence	7.7 %	2.8 %	$-3.0 + 0.8$ %
Compton	5.4 %	5.0 %	2.5 %

Table 1: The systematic, statistical and satellite bunch correction errors for the four methods of the luminosity measurement used in H1 in 1993.

online by separately counting the bremsstrahlung events in the time intervals when the detector is ready to register a new event.

In Table 1 we compare the precision of the four methods of luminosity measurement, achieved in the analysis of 1993 data. The $(e - \gamma)$ coincidence method refers to the online measurements. For all bremsstrahlung methods the systematic errors also include a theoretical uncertainty of 0.5 %, reflecting the accuracy of the Bethe-Heitler formula used in the calculations. The random coincidence and the Compton method precisions are presently limited by the stastistical error, while for the $(e - \gamma)$ coincidence and the hard γ rate method the systematic errors dominate.

The luminosity values obtained using each of the four methods are compared in Fig. 10 for three running periods in 1993. We conclude that all methods give compatible results. The observed agreement of the measured values using largely independent methods gives us confidence that we understand the luminosity measurement, including the satellite bunch correction, at the 4.5 % level in 1993.

In the future we expect to significantly improve the accuracy of the luminosity measurement in H1. Preliminary analyses of the 1994 data show that a precision of 2 % for the hard γ method is attainable while the increased statistics enables us to reduce the size of the errors in the statistics limited methods by a factor of three.
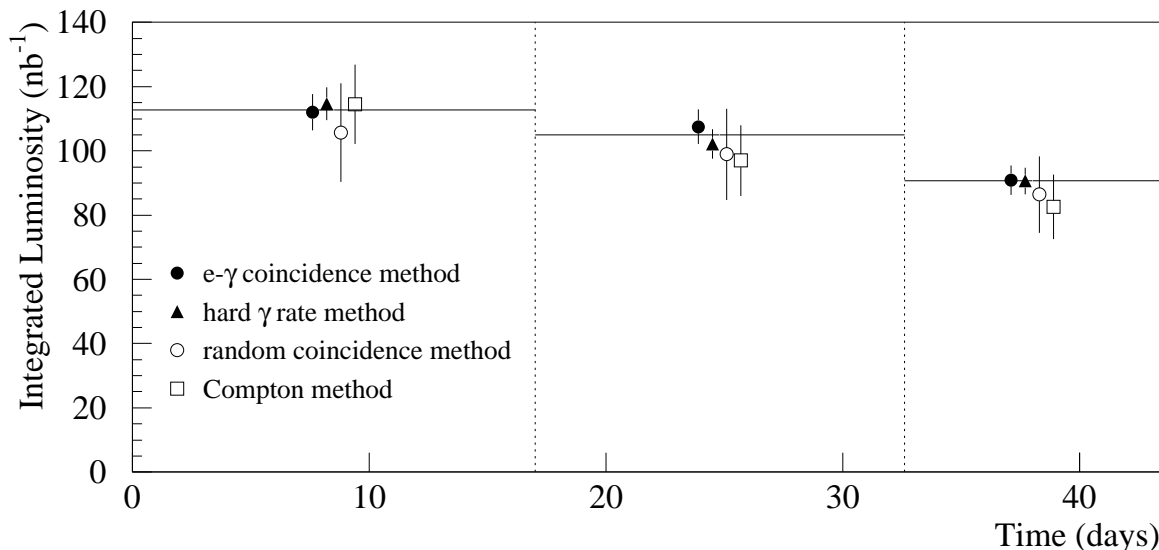

Figure 10: The results of the four luminosity measurements discussed in the text for three run periods in 1993. The error bars correspond to the statistical, systematic and satellite bunch correction errors added in quadrature.

23

6 Experimental check of radiative corrections to DIS

In order to extract the proton structure functions from the inclusive measurement of the deep inelastic differential cross section for the $(\ell p \rightarrow \ell X)$ reaction, the contributions due to higher order electroweak processes have to be calculated and subtracted from the measured distributions. These radiative corrections have given rise to significant systematic uncertainties in the structure functions measured in several DIS fixed target experiments, especially in those using electron beams.

At HERA, the sources of uncertainty are twofold. The first is related to the precision of the calculation and to the knowledge of higher order electroweak corrections to lepton-quark scattering. The corresponding uncertainty is small due to the significant theoretical progress made in this domain [22]. The second and dominant source of uncertainty, affecting the measurements in the large $y_e \gtrsim 0.3$ region, comes from the unknown shape of the structure functions in the unexplored domain of (x, Q^2), especially at $Q^2 \lesssim 4$ GeV^2. Extrapolations of the structure functions to this domain based on QCD [23] or on phenomenological models [24] have to be used to calculate the radiative corrections for the processes which involve the emission of hard photons. The resulting radiative correction uncertainty reflects the arbitrariness of the extrapolation method used and is not very well known.

At HERA, unlike most previous lepton-nucleon scattering experiments, the uncertainty of the radiative corrections can be significantly reduced due to the measurement of the hadronic flow associated with the deep inelastic scattering and to the measurement of hard photons emitted in the direction of the incoming electron. At low y_e (below $\approx$ 0.3) the event kinematics can be reconstructed using the hadronic variables as well as the electronic ones. The corresponding structure functions have different sensitivity to the radiative corrections and their agreement provides a direct cross-check of the radiative corrections.

At larger y_e the method based on the hadronic variables becomes less precise and the event kinematics have to be determined from the electronic variables. In this region hard photon radiation collinear to the incident electron direction is kinematically allowed ($E_\gamma^{max} \leq y_e E_e$) and the radiative correction due to photons of $E_\gamma \simeq E_\gamma^{max}$ dominates the total radiative correction [5]. For a given (x_e, Q_e^2) value this correction is sensitive to the shape of the structure functions in a narrow path in the $(x(E_\gamma), Q^2(E_\gamma))$ plane. For details see [4]. The energy spectrum of radiative photons in the photon detector is sensitive to the assumed form of the structure functions in such a path and provides an experimental cross-check of the corresponding radiative corrections.

In this section we compare the measured and calculated energy spectrum of radiative photons for the event sample selected as described in section 4.3. A similar comparison [25] was made using data collected by the H1 detector in 1992, corresponding to 1/10 of the luminosity available here.

A Monte Carlo simulation of the detector response was used to unfold detector resolution effects. The corresponding corrections are small (up to 20 %). The trigger and vertex finding efficiencies are determined directly from the data. The corresponding efficiency varies as a function of the photon energy in the range from 50 to 80 % and is known with a precision of 10 %. The background due to pileup events is subtracted statistically using the sample of artificially mixed events (see section 4.3). The background contribution is large at the lowest E_γ (30 %) and at the highest E_γ (40 %), and small (7 %)
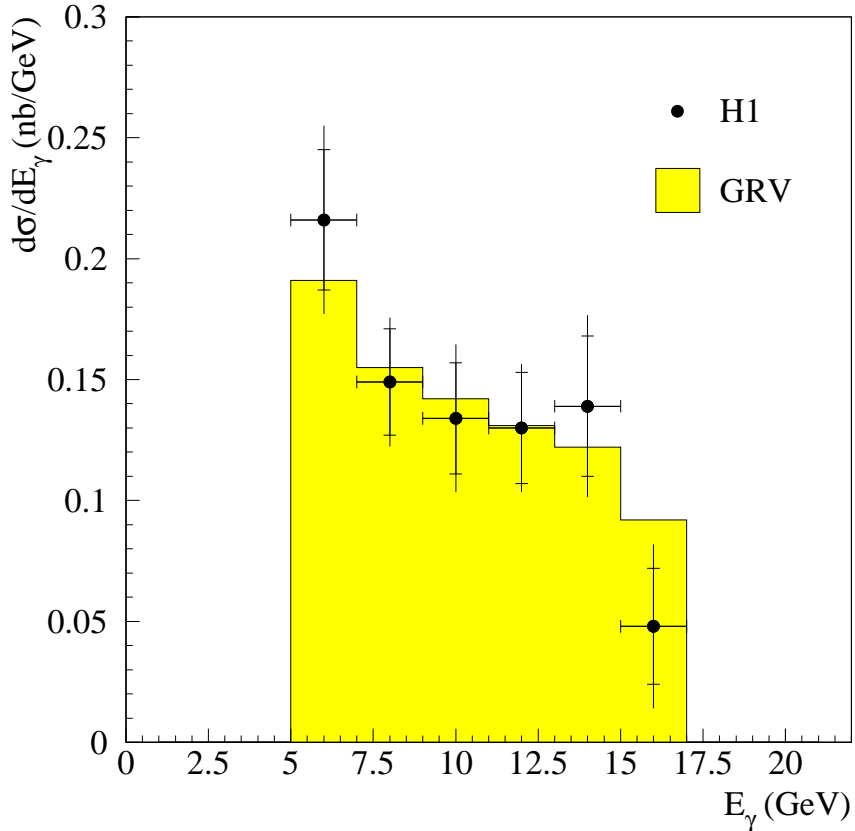
Figure 11: The comparison of the measured (full circles) cross section $d\sigma/dE_\gamma$ for the $ep \rightarrow e\gamma + X$ process, integrated over the kinematic domain defined in the text with the corresponding cross section determined using the HERACLES event generator [27] with the GRV parton distribution parametrizations (shaded area). The inner error bars represent the statistical errors. The full error bars correspond to the statistical and systematic errors added in quadrature. The overall normalization uncertainty related to the luminosity error of 4.5 % is not shown.

around 10 GeV [26] where the acceptance of the electron tagger approaches 100 %. This contribution is known to an accuracy of 25 %. To estimate the systematic error due to a possible miscalibration of the photon detector of 1.5 % we use Monte Carlo methods as in the studies of resolution effects. The resulting error is smaller than 4.5 %.

Fig. 11 shows the cross section $d\sigma/dE_\gamma$ integrated over the kinematic domain specified by the following boundaries: $E'_e > 10$ GeV, $160^\circ \leq \theta_e \leq 172^\circ$ and $\theta'_\gamma \leq 0.45$ mrad. The overall normalization uncertainty related to the luminosity error is 4.5 %. The data is compared to theoretical predictions calculated using the HERACLES program with the parton density parametrization of Glück, Reya and Vogt [23]. The HERACLES program includes all radiative processes to order α^3. The chosen set of parton distributions describe well all available structure function data. Good agreement is observed both in shape and in magnitude, providing an important experimental cross-check of the radiative corrections in the large y_e region with an average error of 25 %. Such a cross-check is of relevance if, in a conservative approach, one does not rely on modelling the proton structure functions in the unmeasured kinematic domain.

7 Probing the proton structure in radiative DIS

As was argued in section 2.4 a radiative deep inelastic scattering event with a hard photon emitted in the direction of the incoming electron can be treated as a non-radiative ep scattering at a reduced centre of mass energy. Thus, with such events, one can measure the proton structure functions at Q^2 values lower by a factor $\approx$ 2 than those attainable using electrons of the nominal beam energy.

The measurement of the radiative photon energy allows us to determine the effective energy of the incoming electron from the equation (10). Subsequently, we reconstruct the event kinematics in terms of x_t and Q_t^2 variables defined by formulae (14) and (16), which describe scattering at a reduced centre of mass energy. At present we are unable, due to small event sample, to measure the double differential cross section and the corresponding structure function F_2. However, we can measure the differential cross section $d\sigma/dQ_t^2$ integrated over $x_t > 2 \cdot 10^{-4}$. The Q_t^2 resolution is typically 10 % and determined primarily by the resolutions of the measured energies of the inelastically scattered electron and of the radiative photon. The differential cross section $d\sigma/dQ_t^2$ is measured in the kinematic region specified by the following boundaries: $E_e' > 10$ GeV, $160^o \leq \theta_e \leq 172^o$, $E_\gamma > 5$ GeV and $\theta_\gamma' \leq 0.45$ mrad. A Monte Carlo simulation of the detector response was used to unfold the detector resolution and geometrical acceptance effects. The event selection efficiencies were determined from the data (see preceding section). The background due to the pileup of deep inelastic and bremsstrahlung events was subtracted statistically. It is present mostly at low Q^2 (corresponding to large E_γ), where it reaches 30 % [26].

In Fig. 12 we show the resulting differential cross section. The errors shown are the statistical (inner bars) and statistical and systematic errors added in quadrature. The statistical errors clearly dominate. The systematic errors include:

- up to 5 % error in the unfolding of the resolution effects,

- up to 20 % error of the event selection efficiency,

- up to 3 % error arising from the energy measurement of the radiative photon and scattered electron,

- up to 10 % error originating from uncertainties in the background subtraction.

The overall normalization error of 4.5 % reflecting the uncertainty in the luminosity measurement is not shown in the figure.

The measured distribution is compared to those calculated using two structure function parametrizations: the GRV parametrization [23] and the MRSD-′ parametrization [29]. The MRSD-′ parametrization is valid down to $Q^2 = 4$ GeV^2. We have used the phenomenological model of [24] to extrapolate the structure functions down to lower Q^2. The observed trend of the data is similar to that calculated using the GRV structure function parametrization.

In order to separate the contribution of transversely and longitudinally polarized photons to the DIS ep inclusive cross section, the variation of the cross section at fixed x and Q^2 as a function of the centre of mass energy has to be measured. Following the method presented in [8] and using the event sample selected in section 4.3 we investigated the possibility of ruling out one of the two extreme hypotheses for the value of $R = \sigma_L/\sigma_T$, namely $R = 0$ and $R = \infty$. In the parton model these two hypotheses can be related to virtual photon scattering off spin 1/2 and spin 0 partons. We found that neither of these hypotheses can be excluded by the presented data.
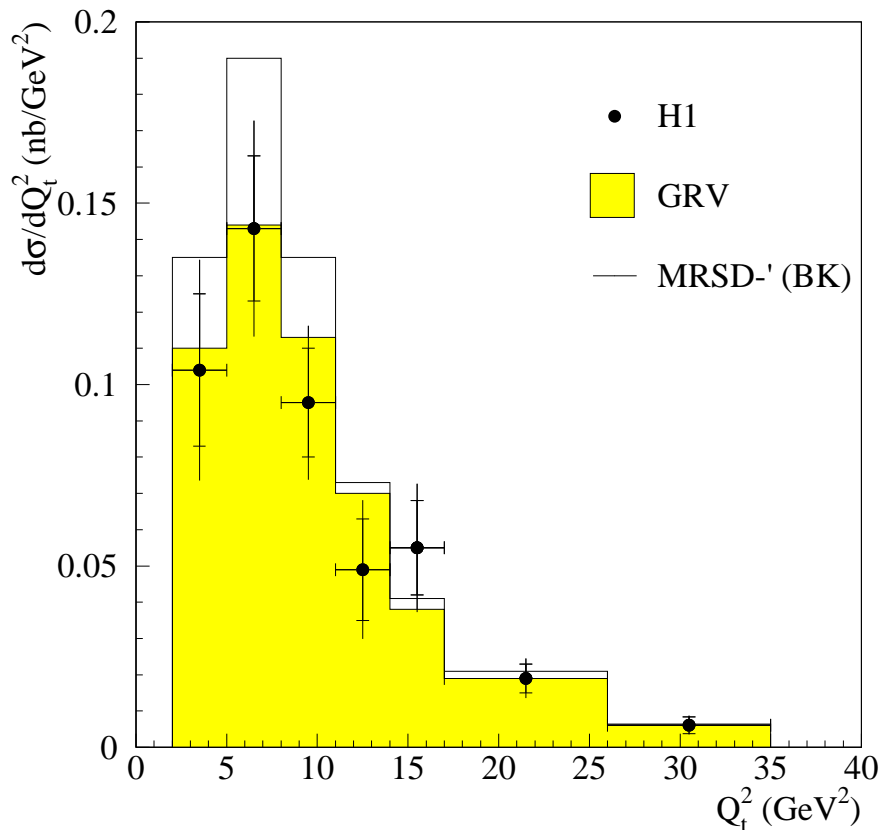
Figure 12: The cross section $d\sigma/dQ_t^2$ for the $ep \rightarrow e\gamma + X$ process, integrated over the kinematic domain definded in the text. The data are represented by full circles with the statistical errors marked by the inner bars and statistical and systematic errors added in quadrature marked as full errors. The shaded area and full line represent the theoretical predictions corresponding to two distinct parametrizations of the structure functions: the GRV and the MRSD-' (BK) [24] sets. These predictions were calculated using the HERACLES event generator. The overall normalization uncertainty related to the luminosity error of 4.5 % is not shown.

8   Conclusions

We have shown that using the H1 detector we can detect and measure the radiative processes $ep \rightarrow e\gamma + p$ and $ep \rightarrow e\gamma + X$ over a large Q^2 range. These processes are employed in order to measure the luminosity. We have demonstrated that 4 largely independent methods of luminosity measurement yield compatible results. From these results we conclude that the integrated luminosity corresponding to the data collected with the H1 detector in 1993 is measured with a precision of 4.5 %. We have measured the spectrum of radiative photons emitted collinearly with respect to the incoming electrons and verified with an accuracy of 25 % the theoretical calculation of the radiative corrections to the differential inclusive DIS cross section. For deep inelastic ep scattering the cross section is measured down to $Q^2 = 2$ GeV^2 using a radiative event sample. The cross section is compatible with that calculated using the GRV parton distributions.

Acknowledgements

References

[1] A. Courau, P. Kessler, Phys. Rev. D 33 (1986) 2028.

[2] L. Suszycki, Proceedings of the HERA workshop, Hamburg October 12-14, 1987, ed. R.D. Peccei, p. 505.

[3] EMC Collaboration, J.J. Aubert et al., Z. Phys. C10 (1981) 101.

[4] M. W. Krasny, Proceedings of the workshop "Physics at HERA", Hamburg October 29-30, 1991, ed. W. Buchmüller and G. Ingelman, p. 850 and references quoted therein.

[5] A. Kwiatkowski, H. Spiesberger, H.J. Möhring, Z. Phys. C50 (1991) 165.

[6] H1 Collaboration, I. Abt et al. Nucl. Phys. B407 (1993) 515.

[7] ZEUS Collaboration, Z. Phys. C63 (1994) 391.

[8] M.W. Krasny, W. Placzek, H. Spiesberger, Z. Phys. C53 (1992) 687.

[9] A. Courau, P. Kessler, Phys. Rev. D46, 117 (1992).

[10] H. Bethe, W. Heitler, Proc. Roy. Soc. A146 (1934) 83.

[11] G.L. Kotkin et al., Z. Phys. C39 (1988) 61.

[12] L.D. Landau, I.Ya. Pomeranchuk, Dokl. Akad. Nauk SSSR 92 (1953) 535.

[13] M. W. Krasny, W. Placzek, Proceedings of the workshop "Physics at HERA", Hamburg October 29-30, 1991, ed. W. Buchmüller and G. Ingelman, p. 862.

[14] H1 Collaboration, The H1 Detector at HERA, DESY preprint 93-103 (1993), to be published in Nucl. Instr. and Methods.

[15] K.I.Avdienko et al., Thallium halides crystals. Production, properties and applications, "Nauka", Novosibirsk, 1989, (in Russian).

[16] H1 Collaboration, T. Ahmed et al., DESY preprint 95-006 (1995), to be published.

[17] H1 Calorimeter Group, B. Andrieu et al., Nucl. Inst. Meth. A336 (1993) 460.

[18] H1 Calorimeter Group, B. Andrieu et al., Nucl. Inst. Meth. A336 (1993) 499.

[19] S. Kermiche, PhD thesis, LAL94-14, 1994.

[20] H1 Collaboration, T. Ahmed et al., Phys. Lett. B340, (1994) 205.

[21] L. Favart, PhD thesis, University of Brussels (1995) in litt.

[22] D.R. Yenni, S.C. Frautchi, H. Suura, Ann. Phys. 13 (1961) 379.
L.W. Mo, Y.S. Tsai, Rev. Mod. Phys. 41 (1969) 205.
D. Bardin et al. Z. Phys. C42 (1989) 679, Z. Phys. C44 (1989) 149.
M. Böhm, H. Spiesberger, Nucl. Phys. B294 (1987) 1081, Nucl. Phys. B304 (1987) 749.
H. Spiesberger et al., Proceedings of the workshop "Physics at HERA", Hamburg October 29-30, 1991, ed. W. Buchmüller and G. Ingelman, p. 798.

[23] M. Glück, E. Reya, A. Vogt, Phys. Lett. B306 (1993) 391.

[24] B. Badelek, J. Kwiecinski, Phys. Lett. B295 (1992) 263.

[25] M. Fleischer, PhD thesis, DESY-FH1K-94-04, 1994.

[26] U. Obrock, PhD thesis, University of Dortmund, 1994.

[27] A. Kwiatkowski, H. Spiesberger, H. J. Möhring, Comp. Phys. Comm. 69 (1992) 155.

[28] N. Y. Volkonsky, L. V. Prokhorov, JETPH Lett. 21 (1975) 389.

[29] A. Martin, W. J. Stirling, R. G. Roberts, Phys. Lett. B306 (1993) 145.